Nature Communications

https://doi.org/10.1038/s41467-026-71295-1

Article in Press

Mitochondrial vulnerability underlies myocarditis from COVID-19 mRNA vaccine

Received: 20 August 2025

Accepted: 18 March 2026

Cite this article as: Mori, G., Yamamoto, M., Ishikawa, K. *et al.* Mitochondrial vulnerability underlies myocarditis from COVID-19 mRNA vaccine. *Nat Commun* (2026). https://doi.org/10.1038/s41467-026-71295-1

Go Mori, Masayoshi Yamamoto, Kaori Ishikawa, Hiroaki Tamashiro, Hayate Suzuki, Seiya Mizuno, Kazuto Nakada & Atsushi Kawaguchi

Title: Mitochondrial vulnerability underlies myocarditis from COVID-19 mRNA vaccine

Authors: Go Mori[1], Masayoshi Yamamoto[2], Kaori Ishikawa[3], Hiroaki Tamashiro[4], Hayate Suzuki[5], Seiya Mizuno[5], Kazuto Nakada[3], and Atsushi Kawaguchi[1,6,7,8,9]*

Addresses:

[1] Graduate School of Comprehensive Human Sciences, University of Tsukuba, Tsukuba 305-8575, Japan

[2] Department of Cardiology, Institute of Medicine, University of Tsukuba, Tsukuba 305-8575, Japan

[3] Institute of Life and Environmental Sciences, University of Tsukuba, Tsukuba 305-8577, Japan

[4] Graduate School of Science and Technology, University of Tsukuba, Tsukuba 305-8577, Japan

[5] Laboratory Animal Resource Center in Transborder Medical Research Center, Institute of Medicine, University of Tsukuba, Tsukuba 305-8575, Japan

[6] Department of Infection Biology, Institute of Medicine, University of Tsukuba, Tsukuba 305-8575, Japan

[7] Transborder Medical Research Center, University of Tsukuba, Tsukuba 305-8575, Japan

[8] Microbiology Research Center for Sustainability, University of Tsukuba, Tsukuba 305-8577, Japan

[9] Center for Quantum and Information Life Sciences, University of Tsukuba, Tsukuba 305-8577, Japan

*Correspondence should be addressed to A.K. (email: ats-kawaguchi@md.tsukuba.ac.jp)

Abstract

mRNA vaccines against SARS-CoV-2 have been widely adopted to combat the COVID-19 pandemic. However, myocarditis has emerged as a rare but severe adverse effect, predominantly affecting young males. Here, we show that mitochondrial vulnerability is associated with mRNA vaccine-associated myocarditis. In our case-control study, patients with postvaccination myocarditis exhibited mitochondrial abnormalities. To examine the impact of mitochondrial damage, mRNA vaccines were administered to *Polg*$^{+/D257A}$ mice, which heterozygously express a proofreading-deficient mitochondrial DNA polymerase that sensitizes mitochondria to stress. mRNA vaccination in *Polg*$^{+/D257A}$ mice reduced left ventricular ejection fraction and induced cardiac immune cell infiltration. Bazedoxifene, a selective estrogen receptor modulator, prevented the reduction of cardiac function in *Polg*$^{+/D257A}$ mice, suggesting a protective role for estrogen signaling. Notably, mRNA vaccination induced mitochondrial reactive oxygen species, resulting in RIPK3 activation, a necroptosis-related kinase, in cardiomyocytes. Collectively, we propose that mitochondrial vulnerability is a potential risk factor for myocarditis following mRNA vaccination, possibly through reactive oxygen species-mediated necroptosis signaling.

Introduction

mRNA vaccines against severe acute respiratory syndrome coronavirus 2 (SARS-CoV-2) have been put into practical use as one of the most effective preventions for coronavirus disease 2019 (COVID-19). The development of mRNA vaccines represents a significant advancement in the fight against the COVID-19 pandemic[1,2]. However, myocarditis has emerged as a rare but severe adverse effect following mRNA vaccination. mRNA vaccine-associated myocarditis typically occurs within a week of vaccination, particularly after a second dose[3]. The incidence is about 1 in 10,000 in males aged 12-30 years and about 1 in 100,000 in the remaining population[4,5]. The young male predominance in the incidence of myocarditis[4.5] may be related to sex hormone differences in the immune response, but the detailed mechanism remains unclear. Histological analysis of endomyocardial biopsy of mRNA vaccine-associated myocarditis patients showed inflammatory infiltrates of lymphocytes, macrophages, and a few eosinophils[6,7]. Specific autoantibodies or particular T cell clones were not observed in mRNA vaccine-associated myocarditis cases[8,9]. In contrast, levels of inflammatory cytokines (interleukin-1β (IL-1β), IL-1RA, and IL-15) and chemokines (C-C motif chemokine ligand 4 (CCL4), C-X-C motif chemokine ligand 1 (CXCL1), and CXCL10) were significantly elevated in the serum of patients[8], suggesting that excessive inflammation may cause myocarditis as a cytokinopathy.

mRNA vaccines are typically based on nucleoside-modified mRNA encapsulated into lipid nanoparticles (LNPs)[10]. The host immune system recognizes unmodified in vitro synthesized mRNA as exogenous molecules through pattern recognition receptors, such as Toll-like receptors (TLRs)[11,12] and RIG-I-like receptors (RLRs)[13,14]. To reduce the activation of the host immune system for the safety and stability of mRNA vaccines, in vitro synthesized mRNA is modified with the cap 1 structure (m^7GpppN_1m) at the 5' end[15] and N^1-methylpseudouridine ($m^1\psi$)[16]. LNPs

currently approved for clinical use are composed of four lipid components: an ionizable cationic lipid (eg, SM-102 and ALC-0315), a phospholipid (eg, DSPC, DOPE), cholesterol, and a polyethylene glycol (PEG)-lipid (eg, DMG-PEG2000). Among these, ionizable lipids have been proposed to elicit endosomal rupture[17], leading to activation of the NOD-like receptor protein 3 (NLRP3) inflammasome[18]. It is also reported that ionizable lipids may have structural similarities to lipopolysaccharides (LPS), allowing them to be recognized by TLR4[19]. However, the components of mRNA vaccines responsible for acute myocarditis remain unknown because no animal model has successfully recapitulated the condition following intramuscular administration of an appropriate vaccine dose.

Here, we identified mitochondrial vulnerability as a potential risk factor for the development of mRNA vaccine-associated myocarditis, based on myocardial biopsy samples from our case-control study and a mouse model using *Polg*$^{+/D257A}$ mice exhibiting subclinical mitochondrial damage. Mitochondria play a pivotal role in energy metabolism and cellular stress responses. Because mitochondrial DNA (mtDNA) exists in multiple copies within a cell, low-level mtDNA damage is functionally compensated by intact mtDNA under basal conditions and remains subclinical. However, upon cellular stress, these compensated defects become unmasked, a state we define as mitochondrial vulnerability. *Polg*$^{+/D257A}$ mice developed cardiac dysfunction upon mRNA vaccination, which was prevented by pharmacological activation of estrogen signaling via a selective estrogen receptor modulator (SERM). Notably, mRNA vaccination induced necroptosis, a form of inflammatory cell death, in cardiomyocytes of *Polg*$^{+/D257A}$ mice. This study provides the first nonoverdose intramuscular mouse model reproducing mRNA vaccine-associated myocarditis and highlights the potential therapeutic targets for preventing this adverse effect.

Results

Case summary of myocarditis after mRNA vaccination

Our case-control study included 6 patients (mean age 22.6 years; 4 males) with myocarditis who exhibited chest pain, fever, myalgia, and fatigue following mRNA vaccination and were hospitalized at the University of Tsukuba Hospital. The patients were categorized as follows: 2 with mild (2 males), 1 with moderate (1 female), and 3 with severe symptoms (2 males, 1 female) (Supplementary Fig. 1a, Supplementary Table 1). The patients with mild symptoms received anti-inflammatory medications such as non-steroidal anti-inflammatory drugs (NSAIDs), prednisolone, and colchicine. The patient with moderate symptoms was treated with anti-arrhythmic drugs and diuretics. The patients with severe symptoms were managed with ventricular assist devices. Three patients received a single dose of the BNT162b2 vaccine, one received 3 doses, and two were vaccinated twice with the mRNA-1273 vaccine. One of the patients with severe symptoms had developed myocarditis due to SARS-CoV-2 infection a year earlier, but the other patients had no pre-existing medical conditions. On average, the symptoms appeared 9.8 days post-vaccination (Supplementary Fig. 1a). All the patients had findings negative for influenza virus, coxsackie virus, SARS-CoV-2, and parvovirus B19. Compared with the healthy controls, all the patients showed increased levels of troponin-T, creatinine kinase MB isotype (CK-MB), and B-type natriuretic peptide (BNP), indicating myocardial tissue damage and impaired cardiac function (Supplementary Fig. 1b-d). The left ventricular ejection fraction (LVEF) in the patients was below the normal threshold of 55%, and in severe cases, it dropped to 10-30% (Supplementary Fig. 1e). The blood leukocyte counts (Supplementary Table 1) and C-reactive protein level (CRP) were also elevated (Supplementary Fig. 1f), indicating the presence of systemic inflammation. Histological analysis of myocardial tissues with hematoxylin and eosin

(HE) staining showed apparent immune cell infiltration and tissue damage with cardiomyocyte vacuolization (Supplementary Fig. 2). These results suggest that, in addition to systemic inflammation, myocarditis also developed following COVID-19 mRNA vaccination, leading to cardiac dysfunction.

Transcriptome analysis of myocardial biopsies

To elucidate the gene expression patterns characteristic of mRNA vaccine-associated myocarditis, we next performed a whole transcriptome analysis using the GeoMx™ Digital Spatial Profiler on formalin-fixed paraffin-embedded (FFPE) myocardial tissues obtained from the patients with mild, moderate, and severe symptoms. Owing to the limited size and availability of myocardial biopsy specimens, multiple sections were prepared from a single FFPE tissue block for each case, and 3-4 ROIs were selected per case. As the control, a FFPE sample obtained from a patient with Löffler syndrome (LS), a form of endocarditis caused by hypereosinophilic syndrome, was also examined. In the severe mRNA vaccine-associated myocarditis case, 208 genes (104 upregulated and 104 downregulated genes) were identified as differentially expressed genes (DEGs) with FDR < 0.05 and fold change ≥ 1.5 or ≤ 0.66 as compared with the LS sample (Fig. 1a, Supplementary Data 1). The mRNA vaccine-associated myocarditis patients showed significantly reduced expression of mitochondria-related genes, including *UQCRB*, *NDUFB1*, *ATP5MC3*, *COX5B*, *COX6A2*, *COX7A1*, and *COX4I1* (Fig. 1a). Hierarchical clustering of these DEGs in the mild, moderate, and severe cases mainly divided them into two clusters (clusters 1 and 2; Fig. 1b). The gene ontology (GO) enrichment analyses for each cluster was performed by using ShinyGO v0.77 (Fig. 1c). Cluster 1 contained DEGs that were upregulated in the severe case, and the associated GO terms were primarily related to the tissue and vascular repair

processes. In contrast, the downregulated DEGs were grouped in cluster 2 and predominantly enriched in pathways related to electron transport chains and oxidative phosphorylation.

Abnormal mitochondrial morphology in myocardial biopsies

Mitochondria are highly dynamic, double-membrane organelles that play a role in energy metabolism and various stress responses, and their morphology is closely linked to function[20]. To examine the mitochondrial abnormalities in myocardial tissues, we next observed the morphological changes of mitochondria by transmission electron microscopy (TEM) (Fig. 2a). In cardiomyocytes, mitochondria are clustered between myofibrils to support high energy demands. Although mitochondrial area were comparable among the LS, immune checkpoint inhibitor (ICI), and mild cases, median mitochondrial areas in the severe cases were 60-70% of those in the LS, ICI, and mild cases (Fig. 2b). Most mitochondria in the LS, ICI, and mild cases exhibited normal morphology with intact mitochondrial outer membranes and well-organized cristae (Fig. 2c). In contrast, the severe cases showed vacuolar degeneration and rupture of the inner mitochondrial membrane (IMM). Moreover, the formation of mitochondria-derived vesicles (MDVs), which bud from damaged or dysfunctional mitochondria[21], was also increased in these patients (Fig. 2c).

mRNA vaccine impairs cardiac function in *Polg*$^{+/D257A}$ mice

To examine whether mitochondrial dysfunction is a causative factor in mRNA vaccine-associated myocarditis, we next examined the adverse effects of mRNA LNPs in mice carrying the D257A heterozygous mutation in the DNA polymerase γ gene (*Polg*$^{+/D257A}$ mice). *Polg* is a nuclear gene encoding the catalytic subunit of mitochondrial DNA polymerase. The D257A mutation in *Polg* reduces 3'-5' exonuclease activity required for proofreading and accumulates

mutations in mtDNA[22,23]. Although *Polg*$^{D257A/D257A}$ mice exhibit a progeroid phenotype, likely owing to severe mitochondrial dysfunction, it is reported that *Polg*$^{+/D257A}$ mice do not show significant defects in body weight, lifespan, and metabolic processes, possibly owing to complementation by the intact *Polg* allele[24,25]. In fact, enzyme histochemistry for cytochrome *c* oxidase (COX; brown) and succinate dehydrogenase (SDH; blue) activities demonstrated that the mitochondrial respiratory capacity of cardiomyocytes in D257A heterozygotes was comparable to that of wild-type (WT), but not in the homozygotes (Supplementary Fig. 3a, b). Given that myocarditis was frequently observed after the first dose of mRNA vaccination in our clinical case-control study (Supplementary Table 1), we next measured the LVEF by echocardiography following single-dose mRNA vaccination (Fig. 3a). Unless otherwise specified in the figure legends, all experiments were conducted using male mice. Baseline LVEF levels were comparable between WT and *Polg*$^{+/D257A}$ mice, averaging approximately 60-70%. However, mRNA-1273 administration reduced the LVEF to below 50% in the *Polg*$^{+/D257A}$ mice, but not in the WT mice. This reduction of cardiac contractility was observed in both male and female *Polg*$^{+/D257A}$ mice 5 days after mRNA vaccination (Supplementary Fig. 4). Moreover, another mitochondrial disease mouse model, mito-miceΔ, which harbor a partial deletion of mitochondrial DNA identical to deletions observed in patients with mitochondrial disease[26], also showed a reduction in LVEF after mRNA-1273 administration (Supplementary Fig. 5). IL-6, a key mediator of the proinflammatory response and a hallmark of cytokine storms, contributes to the innate immune response following mRNA vaccination[27–30]. While plasma IL-6 levels remained unchanged in WT mice, *Polg*$^{+/D257A}$ mice exhibited a significant increase in IL-6 concentration after mRNA-1273 administration (Fig. 3b). These results suggest that mRNA vaccination induces cardiac dysfunction and systemic inflammation in mice with vulnerable mitochondria. This occurs despite

the absence of overt physiological abnormalities before vaccination. Notably, no abnormal COX-SDH staining was observed in the cardiomyocytes of WT and *Polg*$^{+/D257A}$ mice upon intramuscular injection of mRNA-1273 (Fig. 3c, d). These findings suggest that mRNA vaccination reduces cardiac function without impairing mitochondrial respiratory capacity. TEM analysis revealed that approximately 10% of total mitochondria in *Polg*$^{+/D257A}$ cardiomyocytes exhibited ultrastructural abnormalities, such as rupture of the IMM, following mRNA vaccination, whereas no such defects were observed in WT mice (Supplementary Fig. 6). These findings suggest that mRNA vaccination induces mitochondrial damage in cardiomyocytes of *Polg*$^{+/D257A}$ mice. Nevertheless, the mitochondrial respiratory capacity is maintained, possibly through functional compensation by the remaining intact mitochondria (Fig. 3c, d). To evaluate the level of reactive oxygen species (ROS) production, we also examined the nuclear factor erythroid 2-related factor 2 (NRF2)-kelch-like ECH-associated protein 1 (Keap1) and glutathione reductase (GSR) antioxidant pathways as surrogate indicators of oxidative stress in the hearts of *Polg*$^{+/D257A}$ mice (Fig. 3e-g, Supplementary Fig. 7). NRF2 is a transcription factor that regulates the expression of antioxidant genes, while Keap1 is a cytoplasmic repressor that promotes NRF2 degradation under basal conditions. GSR expression tended to increase (Supplementary Fig. 7), and notably, we found a marked upregulation of NRF2 along with degradation of Keap1 (Fig. 3e-g), indicating activation of the NRF2-Keap1 pathway. These results suggest that ROS production is enhanced in the heart following mRNA vaccination in mice with mitochondrial vulnerability. To address the causal link between mitochondrial ROS (mtROS) and reduced cardiac contractility, we treated *Polg*$^{+/D257A}$ mice daily with a mitochondria-specific ROS scavenger, mitoquinone (MitoQ; 2 mg/kg), following mRNA vaccination (Fig. 3h). MitoQ treatment prevented the reduction of cardiac contractility following mRNA vaccination (Fig. 3h). These results suggest

that mtROS generation is a key downstream mediator linking mitochondrial vulnerability to mRNA vaccine-associated myocarditis.

LNPs components cause myocarditis in mice

Although RNA modifications such as $m^1\psi$ and m^7GpppN significantly attenuate immune activation, synthetic mRNA delivered by LNPs can still elicit inflammatory responses through innate immune sensors, including TLRs and RLRs[28–30]. It is also reported that lipid components of LNPs can induce membrane destabilization and endosomal rupture[19], activating the inflammatory response[28]. To determine which component of mRNA-1273 contributes to cardiac dysfunction in *Polg*$^{+/D257A}$ mice, either LNPs without any mRNA (empty LNPs) or Spike capped mRNA modified with $m^1\psi$ were intramuscularly administered (Fig. 4a-d). The administration of Spike mRNA-LNPs, which were formulated in-house using microfluidics with the same components as mRNA-1273, reduced the LVEF of *Polg*$^{+/D257A}$ mice, as observed with mRNA-1273 (Fig. 4b). Importantly, the empty LNPs also impaired the cardiac contractility (Fig. 4c), although to a lesser extent than did in-house Spike mRNA-LNPs (Supplementary Fig. 8). In contrast, no such adverse reaction was observed with mRNA alone (Fig. 4d). As observed with mRNA-1273 (Fig. 3h), the reduction of cardiac contractility induced by either in-house Spike mRNA-LNPs or empty LNPs was consistently ameliorated by MitoQ treatment (Supplementary Fig. 9), indicating that LNP-induced cardiac impairment is mediated by mtROS generation. HE staining of heart slices obtained from *Polg*$^{+/D257A}$ mice showed an interstitial immune cell infiltration following the administration of either mRNA-1273 or empty LNPs (Fig. 4e, f). These results suggest that cellular responses to the lipid components of the mRNA vaccine are one of the causative factors of myocarditis development. Notably, the LVEF was reduced not only by

Spike mRNA-LNPs but also by enhanced green fluorescent protein (EGFP) mRNA-LNPs (Supplementary Fig. 10), indicating that expression of Spike protein is not essential for the development of mRNA vaccine-associated myocarditis.

Protective effect of SERM on myocarditis

Several studies have shown that the incidence of myocarditis after COVID-19 mRNA vaccination is highest for young males[3,4,31]. Androgens (typically associated with males) and estrogens (typically associated with females) are two primary classes of sex hormones that often exert opposing effects. Increased levels of androgens lead to feedback mechanisms that downregulate estrogen production. The level of testosterone, a key androgen, typically peaks in young males and declines with age. To analyze the effect of sex hormones on the sex difference in mRNA vaccine-associated myocarditis, *Polg*$^{+/D257A}$ mice were treated with 3 mg/kg bazedoxifene acetate (BZA) or 10 mg/kg testosterone enanthate (TTE) intraperitoneally for 1 week (Supplementary Fig. 11), and mRNA-1273 was then administered intramuscularly. After the vaccination, mice were further treated with BZA or TTE daily for 5 days (Fig. 5a-c). BZA is a selective estrogen receptor modulator (SERM) that induces dimerization of the estrogen receptor α (ERα)[31] and is primarily used to prevent postmenopausal osteoporosis. TTE is an esterified form of testosterone with a prolonged duration of action. We found that the LVEF was reduced by mRNA-1273 administration in *Polg*$^{+/D257A}$ mice treated with TTE, similarly to the vehicle-treated group (Fig. 5a, b). In contrast, BZA treatment prevented the reduction in cardiac contractility following mRNA vaccination (Fig. 5c).

mRNA vaccine induces necroptosis in the heart

Tissue injury and inflammation are closely associated with the release of damage-associated molecular patterns (DAMPs) from dying cells, which amplify immune responses and exacerbate tissue damage. Among the various forms of regulated cell death, necroptosis plays a critical role in inflammation-driven tissue injury. Necroptosis requires the phosphorylation of RIPK3, which leads to phosphorylation of mixed lineage kinase domain-like protein (MLKL) at serine 345 in mice[33] or at threonine 357/serine 358 in humans[34], causing plasma membrane rupture and subsequent release of DAMPs. Given the potential involvement of necroptosis in mRNA vaccine-associated myocarditis, we next examined the activation of MLKL and the extent of immune cell infiltration using phosphospecific MLKL antibody and anti-CD45 antibody in myocardial tissues obtained from *Polg*$^{+/D257A}$ mice administered mRNA-1273 (Fig. 6a). Following mRNA-1273 administration, phosphorylated MLKL was significantly upregulated in the cytoplasm of necroptotic cardiomyocytes in the *Polg*$^{+/D257A}$ mice compared with the WT mice (Fig. 6a-b). We also observed increased CD45^{+} immune cells (arrowheads) in close proximity to phosphorylated MLKL-positive cardiomyocytes (asterisks) in *Polg*$^{+/D257A}$ mice following mRNA vaccination, compared with WT mice (Fig. 6a, c). RIPK3 expression is downregulated under basal conditions by proteasomal degradation to prevent its inadvertent activation[35]. Upon stimulation with upstream signals such as RIPK1 activation, stabilized RIPK3 undergoes autophosphorylation within the necroptosome, leading to the downstream phosphorylation of MLKL. In the absence of mRNA vaccination, RIPK3 expression was barely detectable in either WT or *Polg*$^{+/D257A}$ mice (Fig. 6d); however, following mRNA vaccination, RIPK3 expression was markedly increased in *Polg*$^{+/D257A}$ mice, but not in WT mice (Fig. 6d, e). Notably, a similar pattern of increased RIPK3 was observed in myocardial biopsy specimens from patients with moderate or severe myocarditis (Fig. 6f, g). To examine the effect of necroptosis on the reduction of cardiac contractility, we

treated *Polg*$^{+/D257A}$ mice with vehicle or 1 mg/kg of RIPK1 and 3 inhibitor, GSK'074, daily following mRNA vaccination (Fig. 6h, Supplementary Fig. 12). GSK'074 treatment prevented the reduction of cardiac contractility following mRNA vaccination (Fig. 6h). These findings suggest that mitochondrial vulnerability increases susceptibility to necroptosis in response to mRNA vaccination and contributes to the development of myocarditis observed in both *Polg*$^{+/D257A}$ mice and human clinical specimens. To further analyze the effect of mtROS on the necroptosis activation, we examined the phosphorylation of MLKL in myocardial tissues from *Polg*$^{+/D257A}$ mice treated with 2 mg/kg MitoQ daily (Fig. 6i, j). Notably, the number of pMLKL-positive cardiomyocytes following mRNA vaccination was significantly reduced in MitoQ-treated mice compared with vehicle-treated mice (Fig. 6i, j). These findings suggest that mitochondrial vulnerability increases susceptibility to oxidative stress, which promotes necroptosis in response to mRNA vaccination and contributes to the development of myocarditis.

DISCUSSION

The heart is one of the most energy-demanding organs, and cardiomyocytes are densely packed with mitochondria, occupying approximately 30% of the cell volume[36]. Disruption of mitochondrial functions, such as energy production, oxidative stress regulation, and cell death control, impairs the homeostasis of the heart, increasing the risk of cardiovascular diseases[37,38]. In our case-control study, patients with mRNA vaccine-associated myocarditis showed abnormal mitochondrial morphology and reduced expression of mitochondria-related genes (Figs. 1 and 2). To test the effect of mitochondrial dysfunction on the development of mRNA vaccine-associated myocarditis, we administered mRNA vaccines to *Polg*$^{+/D257A}$ mice, which carry subclinical mitochondrial damage. Although the cardiac energy production in these mice appeared to be maintained, we observed increased ROS production following mRNA vaccination (Fig. 3). This suggests that mitochondrial vulnerability sensitizes cardiomyocytes to oxidative stress following mRNA vaccination, potentially contributing to the development of myocarditis. Importantly, biodistribution analysis revealed that intramuscularly injected mRNA vaccines remained confined to the injection site and were not detected in the heart (Supplementary Fig. 13), indicating that direct delivery of mRNA to cardiomyocytes is unlikely. Therefore, it is plausible that systemic inflammatory responses triggered by mRNA vaccination, rather than the presence of the Spike mRNA in the myocardium, mediate ROS production and contribute to cardiac injury in susceptible individuals. Cardiotropic viruses have been reported to induce TRIM29 expression and activate PERK-mediated ER stress responses, leading to ROS production that contributes to viral myocarditis[39]. Although it remains unclear whether mRNA vaccination similarly induces TRIM29-PERK signaling, ER stress may represent an upstream trigger of oxidative stress.

A single cell contains not only WT but also mutated mtDNAs, a condition known as heteroplasmy. Mitochondrial dysfunction is generally observed when the proportion of mutated mtDNA exceeds 60-90%. Below this threshold, the WT mtDNA compensates for the defective copies, thereby maintaining mitochondrial function[40]. While ATP production via the mitochondrial electron transport chain (ETC) may be partially maintained through compensation by intact complexes, defective Complex I and III tend to leak electrons, which react with molecular oxygen to generate ROS. The elimination of ROS relies entirely on antioxidant systems such as NRF2. When ROS production overwhelms the capacity of these systems, oxidative stress accumulates and disrupts cellular homeostasis. It has been reported that ROS promote the activation of necroptosis by oxidizing RIP kinases and MLKL[41,42], which enhances their susceptibility to phosphorylation, potentially amplifying the necroptosis signaling induced by mRNA vaccination. Further analysis is needed to elucidate the mechanism of the necroptotic pathway mediated by mitochondrial vulnerability.

The activation of estrogen signaling by BZA, a selective estrogen receptor modulator (SERM), prevents the development of mRNA vaccine-induced myocarditis in *Polg*$^{+/D257A}$ mice (Fig. 5c). BZA binds to ERα and ERβ, which are nuclear hormone receptors mediating estrogen signaling, leading to their dimerization and the subsequent activation of the pathway[32]. Estrogen signaling is known to inhibit inflammatory responses by suppressing the nuclear factor-kappa B (NF-κB) pathway[43] and regulating T cell balance[44]. Notably, BZA has also been proposed to inhibit the IL-6 signaling axis via glycoprotein 130 (gp130), a transmembrane protein that functions as a signal-transducing subunit for cytokine receptors, possibly independent of estrogen signaling[45]. However, given its weak binding activity to gp130 with a Kd value above 140 μM[46,47], the protective effect of BZA against mRNA vaccine-associated myocarditis (Fig. 5c) through

gp130 inhibition may be limited. From another perspective, ERβ is reported to localize to mitochondria via mitochondrial targeting signals within its N-terminal domain, whereas ERα does not[48]. Estrogen has also been reported to maintain mtDNA replication, mitochondrial metabolism, and the morphology by regulating the expression of nuclear-encoded mitochondria-related genes[49-51]. Notably, in female mice, ERα contributed to maintaining cardiac function and cardiomyocyte metabolism through the regulation of mitochondrial activity[52]. Future investigations are required to identify estrogen downstream genes that determine sex differences and to elucidate the distinct functional contributions of ERα and ERβ in mRNA vaccine-associated myocarditis. These findings suggest that estrogen signaling modulation may be of potential value as a preventive or early-intervention strategy, alongside mitochondria-targeted antioxidants or necroptosis inhibitors.

We revealed that the lipid components of the mRNA vaccine contribute to the development of myocarditis in *Polg*$^{+/D257A}$ mice (Fig. 4c). Empty LNPs have been shown to induce IL-1β secretion[28] via membrane destabilization and/or endosomal rupture[17]. It is also reported that the ionizable lipid, SM-102, promotes IL-1β secretion[18,28]. Although the details remain controversial, DMG-PEG2000 lipid, a molecular scaffold ensuring LNP stability, is also implicated in mRNA vaccine-associated hypersensitivity reactions through the production of anti-PEG antibody[53]. To improve the clinical safety of mRNA vaccines, further studies are needed to clarify how empty LNPs induce inflammatory responses.

A number of limitations should be considered when interpreting our results. First, although the gene panel of GeoMx analysis contains over 18,000 nuclear genes, only 8,137 genes were detected owing to reduced RNA quality from the formalin-fixed paraffin-embedded (FFPE) samples (Supplementary Data 1). Unfortunately, key genes related to estrogen signaling and

necroptosis were not observed among them. Second, *Polg*$^{+/D257A}$ mice did not show significant sex-based differences in the LVEF upon mRNA vaccination. Given that mice have a 4 to 5-day estradiol cycle[54], much shorter than that of humans, resulting in no prolonged, sustained elevation of female hormone levels. This may explain the limited sex-dependent sensitivity to mRNA vaccination observed in mice. Despite these limitations, to the best of our knowledge, this is the first study to reproduce mRNA vaccine-associated myocarditis in a mouse model following intramuscular administration of a clinically relevant dose of the mRNA vaccine. *Polg*$^{+/D257A}$ mice will serve as a valuable tool for evaluating the cardiac adverse effects of LNP-mediated therapeutics.

Methods

Study design and participants

This study was conducted as a prospective observation pilot study at the University of Tsukuba Hospital. The participants were recruited from patients hospitalized with acute myocarditis during the period from January 1st, 2018 through August 31st, 2022. The severity of myocarditis was defined according to treatment requirements: mild cases were managed with anti-inflammatory medications, including non-steroidal anti-inflammatory drugs (NSAIDs), prednisolone, and colchicine; moderate case required anti-arrhythmic drugs and diuretics; and severe cases were managed with ventricular assist devices. No viral genomes were detected in any case. This study was conducted in accordance with the Declaration of Helsinki. The protocol was approved by the ethics committee of the University of Tsukuba Hospital (R04-239), and written informed consent was obtained from all the patients. Myocardial specimens were collected from the right ventricular septum via the internal jugular venous approach by using a 7-Fr bioptome (Cordis).

Reagents

Spikevax™ bivalent Original/Omicron BA.4-5 (mRNA-1273; lot# 400212A) was obtained from Moderna. A rabbit anti-phosphorylated MLKL (Ser345) antibody (Cell Signaling Technology; 37333), a rabbit anti-CD45 antibody (abcam; ab10558), a rabbit anti-RIPK3 antibody (Novus Biologicals; NBP2-32257), a mouse anti-NRF2 antibody (Medical & Biological Laboratories; M200-3), a rabbit anti-Keap1 antibody (Cell Signaling Technology; 8047), a mouse anti-lamin A/C antibody (Cell Signaling Technology; 4777), a horseradish peroxidase (HRP)-conjugated anti-rabbit IgG antibody (Cell Signaling Technology; 7074), a HRP-conjugated anti-

mouse IgG antibody (Cell Signaling Technology; 7076), CF®488A Tyramide (biotium; 92171), CF®568 Tyramide (biotium; 92173), Peroxidase Stain DAB Kit (Nacalai; 25985-50), Chemi-Lumi One Super (Nacalai Tesque; 02230), and ImmunoStar LD (Fujifilm; 296-69901) were purchased. Cytokine levels in plasma were measured by using an ELISA kit for mouse IL-6 (R&D Systems; M6000B) according to the manufacturer's protocol.

Transcriptome analysis

Slices of 5 μm in thickness prepared from formalin-fixed paraffin-embedded (FFPE) myocardial tissues were analyzed by the GeoMx Human Whole Transcriptome Atlas panel (> 18,000 genes) according to the manufacturer's protocol. A rabbit anti-laminin antibody conjugated with AlexaFluor 594 (Novus Biologicals; NB300-144AF594) was used as the morphology marker. Owing to the limited size and availability of myocardial biopsy specimens, multiple FFPE myocardial tissue sections were prepared from a single FFPE tissue block per case, and regions of interest (ROIs) containing more than 500 nuclei and morphologically preserved myocardial tissue, free from overt inflammatory damage, were selected (n = 3-4 per case). After the collection of the detection probes, the library was prepared and then sequenced by using the Illumina NovaSeq6000. Gene expression data were analyzed by using GeoMx Analysis Suite and normalized using a third-quartile normalization. Given that GeoMx spatial transcriptomic analysis using FFPE samples generally exhibits smaller expression amplitudes than bulk RNA-seq, fold-change thresholds of ≥ 1.5 or ≤ 0.66 were applied, together with statistical significance (FDR < 0.05), to identify biologically meaningful differentially expressed genes (DEGs). Hierarchical clustering of DEGs between the severe and the Löffler endocarditis cases was performed based on their abundance profiles using the Heatmapper web tool[55]. Clustering was applied to genes

using the average linkage method with Spearman's rank correlation as the distance metric. No additional parameter tuning was performed. Gene Ontology (GO) enrichment analysis was performed on the DEGs of the severe cases and the Löffler endocarditis case via ShinyGO (version 0.77)[56]. An FDR < 0.05 was considered significant for the enrichment terms.

Mice

C57BL/6J mice and their albino variants were purchased from CLEA Japan. Mice were used at 8-10 weeks of age and maintained in a specific pathogen-free facility at the University of Tsukuba with a 12-hour light/12-hour dark cycle, at an ambient temperature of 22 ± 2°C and relative humidity of 50–60%, with ad libitum access to food and water. Both male and female mice were used in this study. The sex of animals used in each experiment is specified in the corresponding figure legends. All in vivo experiments were carried out according to the Guideline for Proper Conduct of Animal Experiments, Science Council of Japan. The protocols for animal experiments were approved by the Animal Care and Use Committee of the University of Tsukuba (25-050). For the construction of gene-modified mice having the D257A mutation in the *Polg* gene, we introduced c.770A>C (p.Asp257Ala) and c.786G>A (p.Arg262Arg) point mutations in the *Polg* gene. The c.786G>A synonymous substitution mutation was included to prevent recleavage during genome editing. The gRNA target (5´-CCT TTG ACC GAG CCC ATA TC-3´) and single-stranded DNA oligonucleotide (ssODN) donor (5´-AGC AGC TCC ACC AAG CAG GAT GGG CAG GAA CAG TTA GTG GTG GGG CAC AAT GTT TCC TTT GCC CGA GCC CAT ATC AGA GAA CAG TAT CTG ATT CAG GTA AGG TTT GTG GGA ATG GAG TGC TGT AAC ATA AGG TGG GCC-3´) were synthesized (Integrated DNA Technologies). In vitro fertilization was performed using the oocytes and sperm obtained from C57BL/6J mice

according to standard protocols. After incubation for 5 h, 2.4 μM Cas9 protein, 3.7 μM crRNA, 7.4 μM tracrRNA, and 100 ng/μl ssODN were electroporated into zygotes by using a NEPA 21 electroporator (NEPAGENE)[57]. The fertilized eggs that had developed to the 2-cell stage were transferred into the oviducts of pseudopregnant ICR females, and newborns were obtained.

Administration of mRNA-LNPs

mRNA-1273 was thawed at room temperature and used within 1 h. The mice were anesthetized by intraperitoneal injection of pentobarbital sodium and administered intramuscularly with a single dose of 10 μl of PBS containing 100 ng or 1 μg of mRNA LNPs into the gastrocnemius muscle. Unless otherwise specified in the figure legends, all experiments were conducted using male mice aged 8-10 weeks. Mice were also intraperitoneally treated with 3 mg/kg bazedoxifene acetate (BZA) (MedchemExpress) or 10 mg/kg testosterone enanthate (TTE) (Fujifilm) dissolved in 100 μl of corn oil, and 1 mg/kg GSK'074 (MedchemExpress), 2 mg/kg MitoQ (Selleck) dissolved in 100 μl of 10% methylcellulose (Fujifilm) containing 0.01% tween-80 (Nacalai).

Preparation of mRNA-LNPs

mRNA encoding the *Spike* gene, *EGFP*, or *Akaluc* gene was synthesized by using T7 RiboMAX RNA synthesis kit (Promega) in the presence of 4 mM CleanCap AG (TriLink BioTechnologies), 5 mM 1-methylpseudouridine (Fujifilm), and 5 mM each of ATP, GTP, and CTP. The synthesized mRNAs were purified through a gel filtration column packed with Sephacryl S-200 HR (Cytiva). mRNA-LNPs were prepared by a microfluidic mixing method using NanoAssemblr Spark (Precision Nanosystems) with lipids containing SM-102 (Echelon

Biosciences): cholesterol (Selleck): 1,2-distearoyl-sn-glycero-3-phosphocholine (DSPC; SIGMA): 1,2-dimyristoyl-rac-glycero-3-methoxypolyethylene glycol-2000 (DMG-PEG2000; MedchemExpress) at molar ratios of 50:38.5:10:1.5 according to the manufacturer's protocol. The resulting mRNA-LNPs were stored at 4°C and used within a few days of 10-fold dilution in PBS.

Transmission electron microscopy (TEM)

The endomyocardial biopsy samples were fixed in 2.5% glutaraldehyde in 100 mM phosphate buffer (pH 7.3) and then fixed in 1% OsO_4 for 30 min at 4°C. After sequential dehydration with ethanol in a stepwise manner, the samples were subjected to propylene oxide treatment and embedded in Epon 812 (Ernest F. Fullam). The ultrathin slices were stained with uranyl acetate and lead citrate and observed by means of transmission electron microscopy (Hitachi; HT7800).

Histological analyses

Mouse tissues were fixed with 10% neutral-buffered formalin for 48 h at room temperature and embedded in paraffin. Three-micrometer slices were subjected to hematoxylin and eosin (HE), immunofluorescence (IF), and immunohistochemical (IHC) staining. Antigen retrieval was conducted by using citrate buffer (pH 6.0) in a pressure cooker for 5 minutes. The slices were blocked with PBS containing 3% BSA and 5% FBS for 30 min at room temperature. The primary antibody diluted in the blocking solution (pMLKL, 1:2000; RIPK3, 1:100; CD45, 1:2000) was incubated overnight at 4˚C. HRP-conjugated secondary antibody was then incubated for 1 h at room temperature. TSA staining solution (PBS-T containing 0.0035% H_2O_2, 1% dextransulfate (SIGMA), 1 μg/ml Tyramide, and 50 ng/ml 4-iodophenol (TCI)) was incubated for

15 min at room temperature, protected from light. For double staining, the antibody was stripped by acidic glycine buffer (pH 2.0). DAB staining was performed according to the manufacturer's protocol. Mitochondrial respiratory activity was assessed in fresh-frozen sections (10 μm thick) prepared from the heart of mice. The cryosections were reacted with 2 mg/mL diaminobenzidine tetrahydrochloride (DOJINDO; 349-00903) in 0.1 M acetate buffer (pH 5.5) containing 0.1% MnCl2 and 0.1% H2O2, followed by incubation with 1 mg/ml of NBT (Fujifilm; 144-01993) in 0.2 M phosphate buffer (pH 7.4) with sodium succinate. When mitochondrial respiratory function is reduced, COX staining (brown) based on the activity of respiratory enzyme complex IV is reduced, and SDH compensates by facilitating redox reactions, resulting in blue-stained cells. The images were obtained by using BZ-X810 (Keyence) or LSM700 (Zeiss). The optical density of the DAB-stained images was measured from the pixel intensity of the DAB stain, which was extracted using ImageJ, and calculated using the following equation[58].

$$\text{Optical density} = -\log_{10}\frac{\text{Mean intensity in ROI}}{\text{Mean intensity in the area wituhout tissue}} \quad (1)$$

The ROI sizes are 100 x 100 μm (Fig. 6e) and 19 x 19 μm (Fig. 6g). The field size is 193 x 193 μm (Fig. 6b, c, and j).

Echocardiography

The mice were anesthetized with isoflurane (3% for induction and 1% while performing measurements). The left ventricular ejection fraction (LVEF) was measured by means of transthoracic echocardiography using a Vevo 2100 (Visual Sonics) system with a 9-70 MHz linear array transducer (MS-550S, v4.5). LVEF was automatically calculated by the system building software (Vevo LAZR v2.2.0, Fujifilm) using the following formula:

$$\text{LVEF}\ (\%) = \frac{\text{LVEDV} - \text{LVESV}}{\text{LVESV}} \times 100 \qquad (2)$$

Each left ventricular volume was automatically estimated by the system building software (Vevo LAZR v2.2.0, Fujifilm) from the end-diastolic dimension (LVDd) and end-systolic dimension (LVDs), measured by the M mode of the parasternal short-axis view. All heart rate data in each echocardiography were provided in Source Data.

Western blot analysis

Heart lysates were prepared in RIPA buffer containing 1 mM PMSF. Proteins were separated on 7.5-10% SDS-PAGE gels and transferred to PVDF membranes (Millipore). Membranes were blocked with 5% milk in TBS-T for 30 min and incubated with primary antibodies (NRF2, 1:1000; Keap1, 1:1000; Lamin A/C, 1:1000) in TBS-T containing 1% milk for 1 h at room temperature, and then with appropriate secondary antibodies. Bands were visualized by using Fusion Solo (Vilber Bio Imaging). The band intensity was measured by ImageJ (version 2.16.0/1.54p).

Quantitative real-time PCR

Total RNA was isolated from WT and *Polg*$^{+/D257A}$ heart by the acid guanidinium phenol chloroform method. cDNA was prepared from 1 μg total RNA by using ReverTraAce (Toyobo) with oligo(dT)$_{20}$ primers. Real-time PCR was carried out using SYBR Green Realtime PCR Master Mix-Plus (Roche) in the Thermal Cycler Dice Real-Time PCR System (TaKaRa). Primer sequences used in this study were as follows: 5'-TCCGTGCCTGGTAGGAAGCC-3' and 5'-

GCAGCGATTGCAACTGGGGT-3' for GSR; 5′-AACGGCTACCACATCCAAGG-3′ and 5′-GGGAGTGGGTAATTTGCGC-3′ for 18S rRNA.

Statistical analysis

Statistical significance was tested by One-way ANOVA with the Tukey test or the unpaired or paired two-tailed Student's t-test using JuppyterLite (version 0.6.3), Python (version 3.12.7), and Graph Pad Prism software (version 7.03). Exact P values are reported in the Source Data file.

Sample size determination

No statistical methods were used to predetermine sample size. For animal experiments, sample sizes were selected based on prior experience with the model and published studies investigating cardiac inflammation and necroptosis in mice, which typically use 4–8 animals per group. These numbers were sufficient to detect biologically relevant differences. For human myocardial biopsy analyses, sample size was constrained by the rarity of clinically confirmed cases. Multiple biopsy sections were analyzed per patient to ensure technical robustness.

Data Availability

Spatial transcriptome data generated in this study have been deposited in the NCBI Gene Expression Omnibus database under accession code GSE316643 (https://www.ncbi.nlm.nih.gov/geo/query/acc.cgi?acc=GSE316643). The gene expression counts are also provided in Supplementary Data 1. Source data are provided with this paper.

References

1. Barda, N. et al. Safety of the BNT162b2 mRNA Covid-19 Vaccine in a Nationwide Setting. *N. Engl. J. Med.* **385**, 1078–1090 (2021).
2. Baden, L. R. et al. Efficacy and Safety of the mRNA-1273 SARS-CoV-2 Vaccine. *N. Engl. J. Med.* **384**, 403–416 (2021).
3. Patone, M. et al. Risks of myocarditis, pericarditis, and cardiac arrhythmias associated with COVID-19 vaccination or SARS-CoV-2 infection. *Nat. Med.* **28**, 410–422 (2022).
4. Pillay, J. et al. Incidence, risk factors, natural history, and hypothesised mechanisms of myocarditis and pericarditis following covid-19 vaccination: living evidence syntheses and review. *BMJ* **378**, e069445 (2022).
5 Ling, R. R. et al. Myopericarditis following COVID-19 vaccination and non-COVID-19 vaccination: a systematic review and meta-analysis. *Lancet Respir. Med.* **10**, 679–688 (2022).
6. Yamamoto, M., Tajiri, K., Ayuzawa, S., & Ieda, M. Pathological findings of clinically suspected myocarditis temporally associated with COVID-19 vaccination. *Eur. J. Heart Fail.* **24**, 1132–1138 (2022).
7. Ammirati, E. et al. Fulminant Myocarditis Temporally Associated with COVID-19 Vaccination. *Curr. Cardiol. Rep.* **26**, 97–112 (2024).
8. Barmada, A. et al. Cytokinopathy with aberrant cytotoxic lymphocytes and profibrotic myeloid response in SARS-CoV-2 mRNA vaccine–associated myocarditis. *Sci. Immunol.* **8**, eadh3455 (2023).
9. Marrama, D., Mahita, J., Sette, A., & Peters, B. Lack of evidence of significant homology of SARS-CoV-2 spike sequences to myocarditis-associated antigens. *EBioMedicine* **75**, 103807 (2022).
10. Qiu, M., Li, Y., Bloomer, H., & Xu, Q. Developing Biodegradable Lipid Nanoparticles for Intracellular mRNA Delivery and Genome Editing. *Acc. Chem. Res.* **54**, 4001–4011 (2021).
11. Heil, F. et al. Species-Specific Recognition of Single-Stranded RNA via Toll-like Receptor 7 and 8. *Science* **303**, 1526–1529 (2004).
12. Diebold, S. S., Kaisho, T., Hemmi, H., Akira, S., & Reis e Sousa, C. Innate Antiviral Responses by Means of TLR7-Mediated Recognition of Single-Stranded RNA. *Science* **303**, 1529–1531 (2004).
13. Yoneyama, M. et al. Shared and Unique Functions of the DExD/H-Box Helicases RIG-I, MDA5, and LGP2 in Antiviral Innate Immunity1. *J. Immunol.* **175**, 2851–2858 (2005).
14. Yoneyama, M. et al. The RNA helicase RIG-I has an essential function in double-stranded RNA-induced innate antiviral responses. *Nat. Immunol.* **5**, 730–737 (2004).

15. Hornung, V. et al. 5’-Triphosphate RNA Is the Ligand for RIG-I. *Science* **314**, 994–997 (2006).

16. Karikó, K., Buckstein, M., Ni, H., & Weissman, D. Suppression of RNA Recognition by Toll-like Receptors: The Impact of Nucleoside Modification and the Evolutionary Origin of RNA. *Immunity* **23**, 165–175 (2005).

17. Omo-Lamai, S. et al. Limiting endosomal damage sensing reduces inflammation triggered by lipid nanoparticle endosomal escape. *Nat. Nanotech*. **20**, 1285–1297 (2025).

18. Ndeupen, S. et al. The mRNA-LNP platform’s lipid nanoparticle component used in preclinical vaccine studies is highly inflammatory. *iScience* **24**, 103479 (2021).

19. Korzun, T. et al. Lipid Nanoparticles Elicit Reactogenicity and Sickness Behavior in Mice Via Toll-Like Receptor 4 and Myeloid Differentiation Protein 88 Axis. *ACS Nano* **18**, 24842–24859 (2024).

20. Kondadi, A. K., Anand, R., & Reichert, A. S. Cristae Membrane Dynamics – A Paradigm Change. *Trends Cell Biol*. **30**, 923–936 (2020).

21. Popov, L.-D. Mitochondrial-derived vesicles: Recent insights. *J. Cell. Mol. Med.* **26**, 3323–3328 (2022).

22. Vanderstraeten, S., Van den Brûle, S., Hu, J., & Foury, F. The Role of 3′-5′ Exonucleolytic Proofreading and Mismatch Repair in Yeast Mitochondrial DNA Error Avoidance. *J. Biol. Chem.* **273**, 23690–23697 (1998).

23. Foury, F., & Vanderstraeten, S. Yeast mitochondrial DNA mutators with deficient proofreading exonucleolytic activity. *EMBO J.* **11**, 2717–2726 (1992).

24. Trifunovic, A. et al. Premature ageing in mice expressing defective mitochondrial DNA polymerase. *Nature* **429**, 417–423 (2004).

25. Kujoth, G. C. et al. Mitochondrial DNA Mutations, Oxidative Stress, and Apoptosis in Mammalian Aging. *Science* **309**, 481–484 (2005).

26. Inoue, K. et al. Generation of mice with mitochondrial dysfunction by introducing mouse mtDNA carrying a deletion into zygotes. *Nat. Genet.* **26**, 176–181 (2000).

27. Alameh, M.-G. et al. Lipid nanoparticles enhance the efficacy of mRNA and protein subunit vaccines by inducing robust T follicular helper cell and humoral responses. *Immunity* **54**, 2877-2892.e7 (2021).

28. Tahtinen, S. et al. IL-1 and IL-1ra are key regulators of the inflammatory response to RNA vaccines. *Nat. Immunol.* **23**, 532–542 (2022).

29. Kim, S. et al. Innate immune responses against mRNA vaccine promote cellular immunity through IFN-β at the injection site. *Nat. Commun.* **15**, 7226 (2024).

30. Li, C. et al. Mechanisms of innate and adaptive immunity to the Pfizer-BioNTech BNT162b2 vaccine. *Nat. Immunol.* **23**, 543–555 (2022).

31. Block, J. P. et al. Cardiac Complications After SARS-CoV-2 Infection and mRNA COVID-19 Vaccination — PCORnet, United States, January 2021–January 2022. *MMWR Morb. Mortal. Wkly. Rep.* **71**, 517-523 (2022).

32. Lewis-Wambi, J. S. et al. The Selective Estrogen Receptor Modulator Bazedoxifene Inhibits Hormone-Independent Breast Cancer Cell Growth and Down-Regulates Estrogen Receptor α and Cyclin D1. *Mol. Pharmacol.* **80**, 610–620 (2011).

33. Rodriguez, D. A. et al. Characterization of RIPK3-mediated phosphorylation of the activation loop of MLKL during necroptosis. *Cell Death Differ.* **23**, 76–88 (2016).

34. Sun, L. et al. Mixed Lineage Kinase Domain-like Protein Mediates Necrosis Signaling Downstream of RIP3 Kinase. *Cell* **148**, 213–227 (2012).

35. Choi, S.-W. et al. PELI1 Selectively Targets Kinase-Active RIP3 for Ubiquitylation-Dependent Proteasomal Degradation. *Mol. Cell* **70**, 920-935.e7 (2018).

36. Li, K. et al. Mitochondrial dysfunction in cardiovascular disease: Towards exercise regulation of mitochondrial function. *Front. Physiol.* **14**, 1063556 (2023).

37. Suliman, H. B., & Piantadosi, C. A. Mitochondrial Quality Control as a Therapeutic Target. *Pharmacol. Rev.* **68**, 20–48 (2016).

38. Lesnefsky, E. J., Chen, Q., & Hoppel, C. L. Mitochondrial Metabolism in Aging Heart. *Circ. Res.* **118**, 1593–1611 (2016).

39. Wang, J. et al. Loss of TRIM29 mitigates viral myocarditis by attenuating PERK-driven ER stress response in male mice. *Nat. Commun.* **15**, 3481 (2024).

40. Nakada, K. et al. Inter-mitochondrial complementation: Mitochondria-specific system preventing mice from expression of disease phenotypes by mutant mtDNA. *Nat. Med.* **7**, 934–940 (2001).

41. Deragon, M. A. et al. Mitochondrial ROS prime the hyperglycemic shift from apoptosis to necroptosis. *Cell Death Discov.* **6**, 132 (2020).

42. Zhang, Y. et al. RIP1 autophosphorylation is promoted by mitochondrial ROS and is essential for RIP3 recruitment into necrosome. *Nat. Commun.* **8**, 14329 (2017).

43. Stein, B., & Yang, M. X. Repression of the Interleukin-6 Promoter by Estrogen Receptor Is Mediated by NF-κB and C/EBPβ. *Mol. Cell. Biol.* **15**, 4971–4979 (1995).

44. Maglione, A., Rolla, S., Mercanti, S. F., Cutrupi, S., & Clerico, M. The Adaptive Immune System in Multiple Sclerosis: An Estrogen-Mediated Point of View. *Cells* **8**, 1280 (2019).

45. Li, H. et al. Drug Design Targeting Protein–Protein Interactions (PPIs) Using Multiple Ligand Simultaneous Docking (MLSD) and Drug Repositioning: Discovery of Raloxifene and Bazedoxifene as Novel Inhibitors of IL-6/GP130 Interface. *J. Med. Chem.* **57**, 632–641 (2014).

46. Song, D. et al. Discovery of bazedoxifene analogues targeting glycoprotein 130. *Eur. J. Med. Chem.* **199**, 112375 (2020).

47. Park, S. A., Kim, L. K., Park, H. M., Kim, H. J., & Heo, T. H. Inhibition of GP130/STAT3 and EMT by combined bazedoxifene and paclitaxel treatment in ovarian cancer. *Oncol. Rep.* **47**, 52 (2022).

48. Yang, SH. et al. Mitochondrial localization of estrogen receptor beta. *Proc. Natl. Acad. Sci. U.S.A.* **101**, 4130-4135 (2004).

49. Sastre-Serra, J., Nadal-Serrano, M., Pons, D. G., Roca, P., & Oliver, J. Mitochondrial dynamics is affected by 17β-estradiol in the MCF-7 breast cancer cell line. Effects on fusion and fission related genes. *Int. J. Biochem. Cell Biol.* **44**, 1901–1905 (2012).

50. Klinge, C. M. Estrogenic control of mitochondrial function. *Redox Biol.* **31**, 101435 (2020).

51. Ribas, V. et al. Skeletal muscle action of estrogen receptor α is critical for the maintenance of mitochondrial function and metabolic homeostasis in females. *Sci. Transl. Med.* **8**, 334ra54 (2016).

52. Tham, YK. et al. Estrogen receptor alpha deficiency in cardiomyocytes reprograms the heart-derived extracellular vesicle proteome and induces obesity in female mice. *Nat. Cardiovasc. Res*. **2**, 268-289 (2023).

53. Ju, Y. et al. Anti-PEG Antibodies Boosted in Humans by SARS-CoV-2 Lipid Nanoparticle mRNA Vaccine. *ACS Nano* **16**, 11769–11780 (2022).

54. Quignon, C. Collection and Analysis of Vaginal Smears to Assess Reproductive Stage in Mice. *Curr. Protoc.* **3**, e887 (2023).

55. Babicki, S. et al. Heatmapper: web-enabled heat mapping for all. *Nucleic Acids Res.* **44**, W147-153 (2016).

56. Ge, S. X., Jung, D., & Yao, R. ShinyGO: a graphical gene-set enrichment tool for animals and plants. *Bioinforma. Oxf. Engl.* **36**, 2628–2629 (2020).

57. Tamari, T. et al. A universal method for generating knockout mice in multiple genetic backgrounds using zygote electroporation. *Biol. Open* **12**, bio059970 (2023).

58. Patera, F., Cudzich-Madry, A., Huang, Z., & Fragiadaki, M. Renal expression of JAK2 is high in polycystic kidney disease and its inhibition reduces cystogenesis. *Sci. Rep.* **9**, 4491 (2019).

ACKNOWLEDGMENTS

We thank Flaminia Miyamasu (Medical English Communications Center, University of Tsukuba) for grammatical revision of the manuscript. We also thank the investigators at the University of Tsukuba Hospital for specimen collection. This work was supported in part by grants-in-aid from the Ministry of Education, Culture, Sports, Science and Technology of Japan (23K24136 and 25K22548 to A.K., 22H02536 and 23K23801 to K.N.); the Research Program on Emerging and Re-emerging Infectious Diseases (JP20fk0108076 and JP24fk0108691 to A.K., JP22fk0108638 to A.K. and S.M.); the Japan Program for Infectious Diseases Research and Infrastructure (JP20wm0325019 and JP23wm0325062 to A.K.); AMED-CREST (JP22gm1610008 to A.K., JP23gm1110006 to K.N.) from the Japan Agency for Medical Research and Development; the JST FOREST Program (JPMJFR204M to K.I.); JST SPRING (JPMJS2124 to G.M. and H.T.); COI-NEXT (JPMJPF2017 to A.K.) from the Japan Science and Technology Agency; the Shionogi Infectious Disease Research Promotion Foundation (2310T00100 to A.K.); and the Takeda Science Foundation (2505T00093 to A.K.).

Author contributions statement

G.M. and A.K. conceived and designed the experiments; G.M., K.I., H.T., and A.K. performed the experiments; G.M., K.I., K.N., and A.K. analyzed the data; M.Y., H.S., S.M., K.I., K.N., and A.K. provided the biological materials; and G.M., K.I., S.M., and A.K. wrote the manuscript.

Competing interests statement

The authors declare no competing interests.

Overlapping publication

The human myocardial tissues included in this study were also used in a previous publication as a case report (mild case-1, moderate case, and severe case-2)[6]. The current study provides additional cases and performs further analyses to investigate the molecular mechanism underlying mRNA vaccine-associated myocarditis, which were not included in the previous publication.

Figure legends

Figure 1 Down-regulation of mitochondria-related nuclear genes in mRNA vaccine-associated myocarditis. (**a**) Volcano plot comparing gene expression between a severe mRNA vaccine-associated case and a Löffler syndrome (LS) case. The x-axis represents the $\log_2$ fold change, and the y-axis, the $-\log_{10}$ adjusted P-value (Benjamini-Hochberg false discovery rate, FDR). Two-tailed, unpaired Student's t-test (severe, n = 3 biopsies; LS, n = 4 biopsies). Differentially expressed genes were defined as ≥ 1.5-fold upregulation or ≤ 0.66-fold downregulation with FDR < 0.05 (red dots). Mitochondrial-related genes are shown in blue. A representative field-of-view image showing myocardial tissue morphology with laminin staining used for ROI selection is shown. Source data are provided as a Supplementary Data 1. Scale bar, 250 μm. (**b**) Heatmap of 208 DEGs across the mild, moderate, and severe cases and the Löffler endocarditis case (n = 3 ROIs for mild, moderate, and severe cases, n = 4 ROIs for LS). Green represents lower expression levels, and magenta, higher expression levels. The columns represent individual samples, and the rows, genes. The values of each gene expression level are shown in Supplementary Data 1. (**c**) GO analysis of gene clusters identified in (**b**). The bars indicate the fold enrichment, the color intensity, and statistical significance ($-\log_{10}$ FDR).

Figure 2 Morphological abnormalities of mitochondria in mRNA vaccine-associated myocarditis cases. (**a**) Transmission electron microscope images of myocardial tissue biopsied from mild case-1, moderate case, severe case-1, and severe case-3. Scale bar, 1 μm. (**b**) Violin plot of the individual mitochondrial areas of the LS case (n = 87 mitochondria), ICI case (n = 70 mitochondria), mild case-1 (n = 50 mitochondria), moderate case (n = 47 mitochondria), severe case-1 (n = 71 mitochondria), and severe case-3 (n = 118 mitochondria). Mitochondria represent

technical subsampling within each patient sample. Because the number of independent patients per group was limited, no statistical test was performed for between-group comparisons. The centre line indicates the median, the box limits indicate interquartile range (IQR; 25th-75th percentiles), and the whiskers extend to 1.5 x IQR. (**c**) Percentage of normal (dark blue), normal-vacuolar (light blue), vacuolar (yellow), ruptured (orange) mitochondria, and mitochondria-derived vesicles (MDVs; red) in myocardial tissues. Percentages are expressed as a ratio of each category to the total number of mitochondria counted. Representative images are shown (**a**, **c**). Similar findings were observed across all biopsy sections analyzed (LS, n = 4; ICI, n = 4; mild-1, n = 4; moderate, n = 6; severe-1, n = 2; severe-3, n = 6). Scale bar, 200 nm. Source data are provided as a Source Data file.

Figure 3 mRNA vaccination causes cardiac dysfunction in *Polg*$^{+/D257A}$ mice. (**a**) Violin plot of LVEF at 5 days post-administration of 100 ng mRNA-1273 in WT and *Polg*$^{+/D257A}$ mice (n = 9 for WT and mock *Polg*$^{+/D257A}$, n = 11 for mRNA-1273 *Polg*$^{+/D257A}$). (**b**) Plasma IL-6 levels at 6 h post-administration of 1 μg mRNA-1273 in WT and *Polg*$^{+/D257A}$ mice (n = 9 for mock WT, n = 7 for mRNA-1273 WT, n = 8 for mock *Polg*$^{+/D257A}$, n = 6 for mRNA-1273 *Polg*$^{+/D257A}$). (**c, d**) Cytochrome *c* oxidase (COX; brown) and succinate dehydrogenase (SDH; blue) staining were performed on myocardial tissues from WT and *Polg*$^{+/D257A}$ mice at 5 days post-vaccination with 100 ng mRNA-1273. Scale bar, 100 μm (**c**). The ratio of the COX-positive cardiomyocytes was examined per 50 cardiomyocytes (**d;** n = 8 biologically independent mice). (**e-g**) Western blots of NRF2 and Keap1 in the heart from WT and *Polg*$^{+/D257A}$ mice were conducted at 5 days post-vaccination with 100 ng mRNA-1273 (**e**). Lamin A/C was used as the loading control. The relative intensities of NRF2 and Keap1 were normalized to lamin A/C (**f**; n = 4 for WT, n = 5 for *Polg*$^{+/D257A}$,

g; n = 5 for WT, n = 6 for mock *Polg*$^{+/D257A}$, n = 4 for mRNA-1273 *Polg*$^{+/D257A}$, biologically independent mice). (**h**) LVEF was measured at 0 and 5 days post-administration of mRNA-1273 in *Polg*$^{+/D257A}$ mice treated daily with vehicle (n = 6) and 2 mg/kg MitoQ (n = 9). All experiments were performed using male mice aged 8-10 weeks. The centre line indicates the median, the box limits indicate IQR (25th-75th percentiles), and the whiskers extend to 1.5 x IQR (**b, d, f, g, h**). Two-tailed, paired Student's t-test (**h**). One-way ANOVA with Tukey's test (**a**, **b**, **d, f, g**). Source data are provided as a Source Data file.

Figure 4 Lipid nanoparticle components cause myocarditis in *Polg*$^{+/D257A}$ mice. (**a-d**) LVEF was examined in *Polg*$^{+/D257A}$ mice administered 100 ng of mRNA-1273 (**a**; n = 6), 100 ng of in-house-prepared Spike mRNA-LNPs (**b**; n = 11), an equivalent amount of empty-LNPs containing the same lipids as mRNA-1273 (**c**; n = 12), or 100 ng of Spike mRNA (**d**; n = 7) at 0 and 5 days post-administratoin. (**e, f**) HE staining of myocardial tissues at 5 days post-administration of PBS, mRNA-1273, or empty-LNPs in *Polg*$^{+/D257A}$ mice; Scale bar, 100 μm (**e**). The counts of immune cells per ROI (100 x 100 μm) (**f**; n = 7 for PBS, n = 6 for mRNA-1273, empty LNPs). All experiments were performed using male mice aged 8-10 weeks. n represents biologically independent mice. The centre line indicates the median, the box limits indicate IQR (25th-75th percentiles), and the whiskers extend to 1.5 x IQR (**a-d, f**). Two-tailed, paired Student's t-test (**a-d**). One-way ANOVA with Tukey's test (**f**). Source data are provided as a Source Data file.

Figure 5 SERM ameliorates cardiac dysfunction following mRNA-1273 administration. (**a-c**) LVEF was measured at 0 and 5 days post-administration of mRNA-1273 in *Polg*$^{+/D257A}$ mice treated with vehicle (**a**; n = 6), testosterone enanthate (TTE) (**b**; n = 5), or bazedoxifene acetate

(BZA) (**c**; n = 6). n represents biologically independent mice. All experiments were performed using male mice aged 8-10 weeks. The centre line indicates the median, the box limits indicate IQR (25th-75th percentiles), and the whiskers extend to 1.5 x IQR (**a-c**). Two-tailed, paired Student's t-test (**a-c**). Source data are provided as a Source Data file.

Figure 6 Mitochondrial vulnerability predisposes cardiomyocytes to necroptosis upon mRNA-1273 vaccination. (**a-c**) Immunofluorescence staining of cardiac sections for phosphorylated MLKL (Ser345; green) and CD45 (magenta) at 5 days post-vaccination with 100 ng mRNA-1273 in WT or *Polg*$^{+/D257A}$ mice (**a**). Scale bar, 20 μm; enlarged image, 10 μm. Quantification of pMLKL-positive cells to the total number of cells per field (**b**; n = 6 for WT and PBS *Polg*$^{+/D257A}$, n = 7 for mRNA-1273 *Polg*$^{+/D257A}$) and CD45-positive cells per field (**c**; n = 3 for PBS WT and *Polg*$^{+/D257A}$, n = 5 for mRNA-1273 WT, n = 8 for mRNA-1273 *Polg*$^{+/D257A}$). (**d, e**) Immunohistochemistry for RIPK3 at 5 days post-vaccination with 100 ng mRNA-1273 in WT or *Polg*$^{+/D257A}$ mice (**d**). Scale bar, 100μm. Quantification of mean DAB optical density per ROI (**e**; n = 8 for mRNA-1273 WT and *Polg*$^{+/D257A}$, n = 7 for PBS *Polg*$^{+/D257A}$). (**f, g**) RIPK3 immunohistochemistry in myocardial biopsies from the LS, moderate, and severe cases (**f**) with quantification per ROI (**g**; n = 400 ROIs for LS and moderate, n = 353 ROIs for severe). ROIs represent technical subsampling within each patient. Because the number of independent patients per group was limited, no statistical test was performed for between-group comparisons. Scale bar, 100 μm. (**h**) LVEF was measured at 0 and 5 days post-administration of mRNA-1273 in *Polg*$^{+/D257A}$ mice treated daily with vehicle (n = 6) and GSK'074 (n = 6). (**i, j**) Immunofluorescence for phosphorylated MLKL (Ser345, green) in *Polg*$^{+/D257A}$ mice treated with vehicle or MitoQ at 5 days post-vaccination with 100 ng mRNA-1273 (**i**) and quantification of pMLKL-positive cells

to the total number of cells per field (**j**, n = 4). Scale bar, 20 µm. All experiments were performed using male mice aged 8-10 weeks. The centre line indicates the median, the box limits indicate IQR (25th-75th percentiles), and the whiskers extend to 1.5 x IQR (**b, c, e, h, j**). n represents biologically independent mice. Two-tailed, paired Student's t-test (**h**). One-way ANOVA with Tukey's test (**b, c, e, j**). Source data are provided as a Source Data file.

Editorial summary:

This study shows that mitochondrial vulnerability increases the risk of myocarditis after mRNA vaccination by promoting inflammatory cell death in cardiomyocytes, identifying a potential mechanism underlying rare but severe cardiac adverse events.

Peer review information: *Nature Communications* thanks Junji Xing, Stephen Kent, Yu Feng, and the other, anonymous, reviewer(s) for their contribution to the peer review of this work. A peer review file is available.

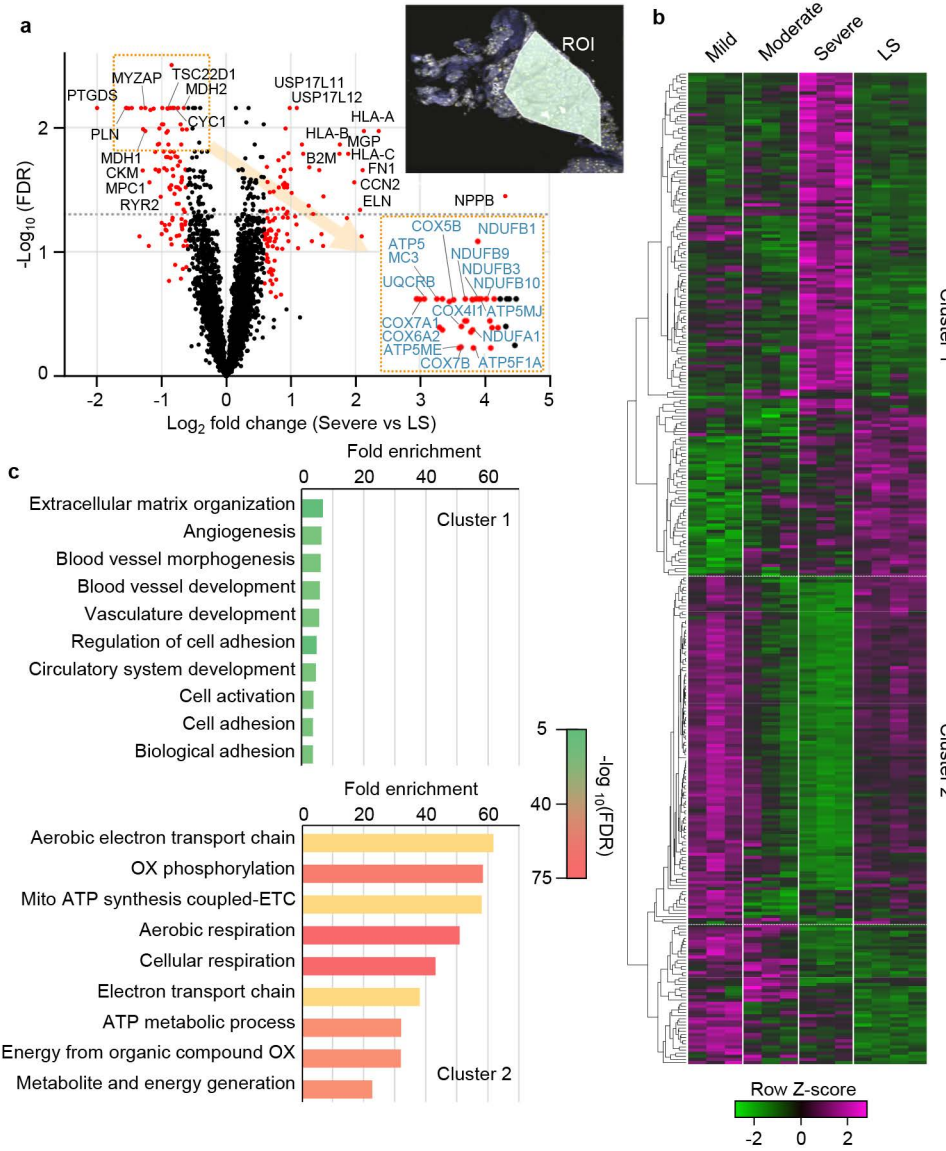
a
ROI
MYZAP
TSC22D1
MDH2
PTGDS
CYC1
PLN
MDH1
CKM
MPC1
RYR2
USP17L11
USP17L12
HLA-A
HLA-B
MGP
B2M
HLA-C
FN1
CCN2
ELN
NPPB
COX5B
NDUFB1
ATP5
MC3
NDUFB9
NDUFB3
UQCRB
NDUFB10
COX4I1
ATP5MJ
COX7A1
COX6A2
NDUFA1
ATP5ME
COX7B
ATP5F1A
-Log10 (FDR)
Log2 fold change (Severe vs LS)
b
Mild
Moderate
Severe
LS
Cluster 1
Cluster 2
Row Z-score
-2
0
2
c
Fold enrichment
Extracellular matrix organization
Angiogenesis
Blood vessel morphogenesis
Blood vessel development
Vasculature development
Regulation of cell adhesion
Circulatory system development
Cell activation
Cell adhesion
Biological adhesion
Cluster 1
-log 10(FDR)
Aerobic electron transport chain
OX phosphorylation
Mito ATP synthesis coupled-ETC
Aerobic respiration
Cellular respiration
Electron transport chain
ATP metabolic process
Energy from organic compound OX
Metabolite and energy generation
Cluster 2

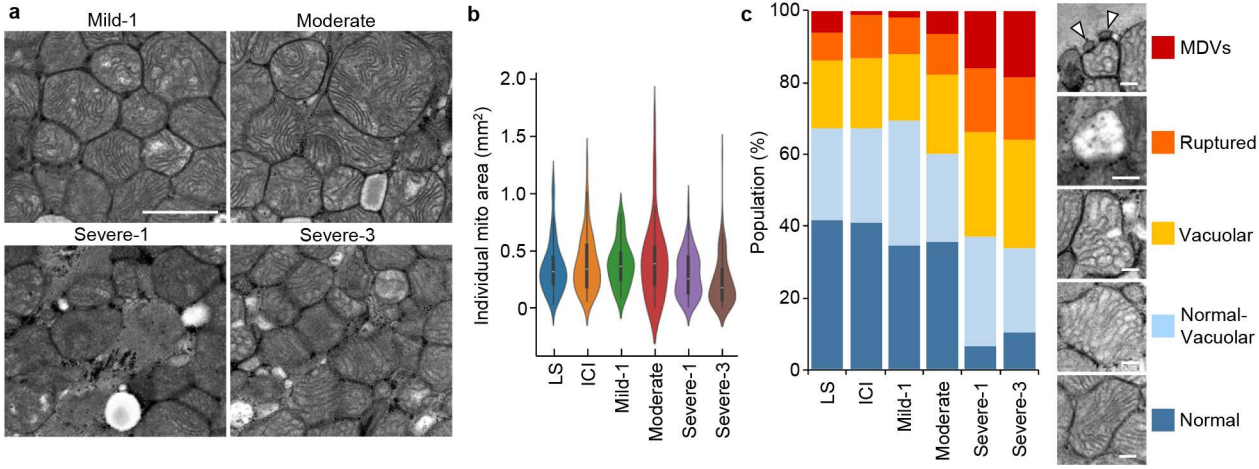

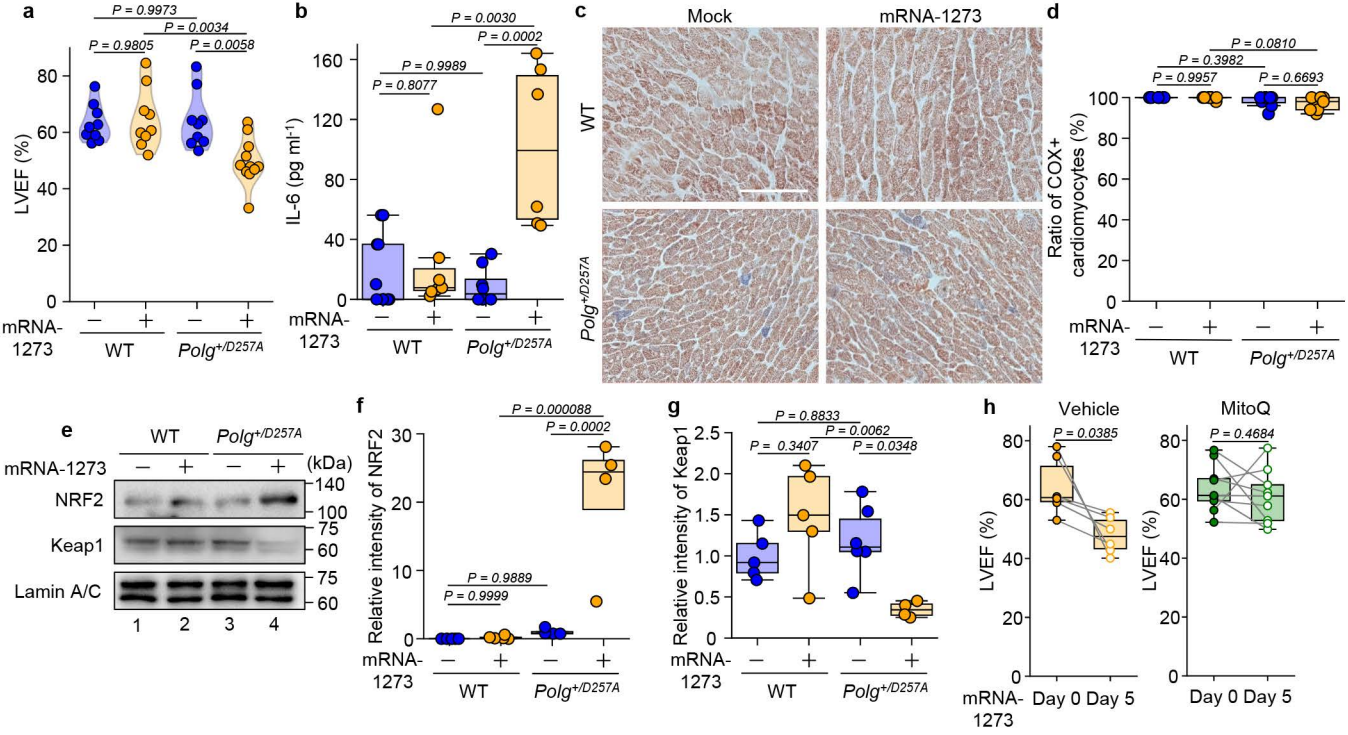
a
P = 0.9973
P = 0.0034
P = 0.9805
P = 0.0058
LVEF (%)
mRNA-1273
WT
Polg+/D257A
b
P = 0.0030
P = 0.0002
P = 0.9989
P = 0.8077
IL-6 (pg ml-1)
c
Mock
mRNA-1273
WT
Polg+/D257A
d
P = 0.0810
P = 0.3982
P = 0.9957
P = 0.6693
Ratio of COX+ cardiomyocytes (%)
e
(kDa)
NRF2
Keap1
Lamin A/C
f
P = 0.000088
P = 0.0002
P = 0.9889
P = 0.9999
Relative intensity of NRF2
g
P = 0.8833
P = 0.0062
P = 0.3407
P = 0.0348
Relative intensity of Keap1
h
Vehicle
MitoQ
P = 0.0385
P = 0.4684
LVEF (%)
Day 0
Day 5

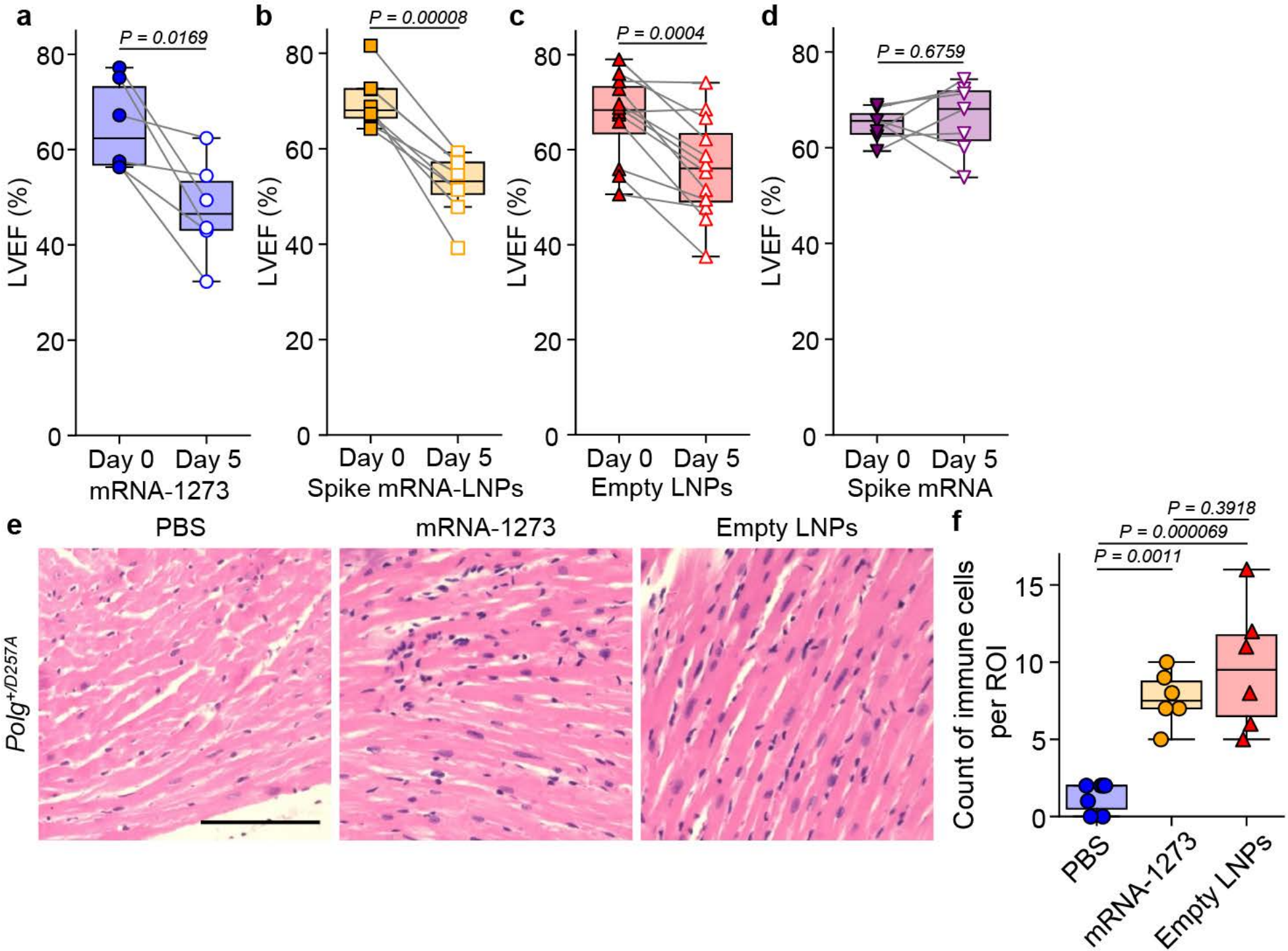

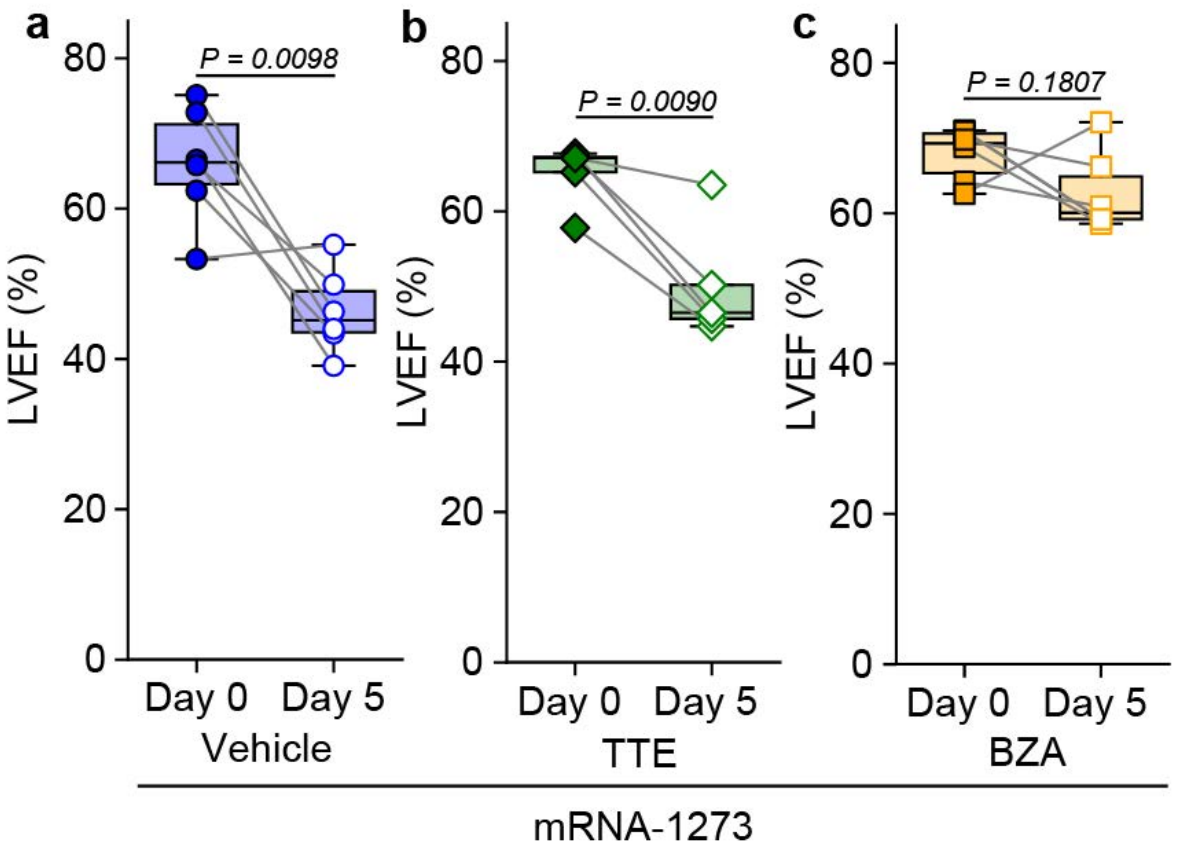

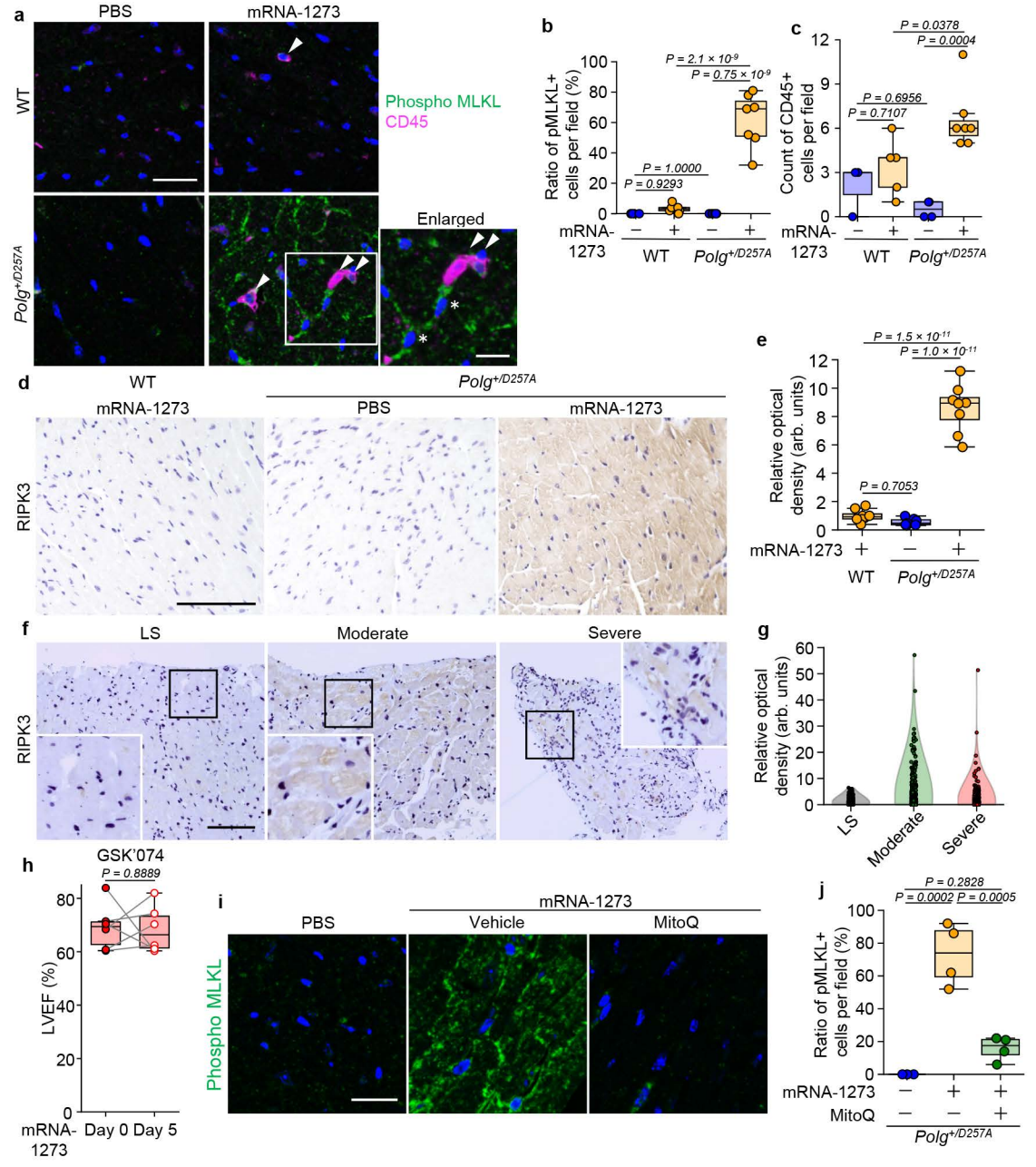
a
PBS
mRNA-1273
WT
Polg+/D257A
Phospho MLKL
CD45
Enlarged
b
Ratio of pMLKL+ cells per field (%)
P = 2.1 × 10-9
P = 0.75 × 10-9
P = 1.0000
P = 0.9293
mRNA-1273
WT
Polg+/D257A
c
Count of CD45+ cells per field
P = 0.0378
P = 0.0004
P = 0.6956
P = 0.7107
d
WT
Polg+/D257A
mRNA-1273
PBS
RIPK3
e
Relative optical density (arb. units)
P = 1.5 × 10-11
P = 1.0 × 10-11
P = 0.7053
f
LS
Moderate
Severe
g
Relative optical density (arb. units)
h
GSK'074
P = 0.8889
LVEF (%)
Day 0
Day 5
i
PBS
mRNA-1273
Vehicle
MitoQ
Phospho MLKL
j
Ratio of pMLKL+ cells per field (%)
P = 0.2828
P = 0.0002
P = 0.0005
MitoQ